

Optical, Thermal, and Mechanical Properties of (Y_{1-x}Sc_x)₂O₃ Transparent Ceramics

Jiquan Huang (✉ hjq@fjirsm.ac.cn)

Chinese Academy of Sciences Fujian Institute of Research on the Structure of Matter
<https://orcid.org/0000-0002-3983-3400>

Changliang YANG

Chinese Academy of Sciences Fujian Institute of Research on the Structure of Matter

Qiufeng HUANG

Chinese Academy of Sciences Fujian Institute of Research on the Structure of Matter

Zhonghua DENG

Chinese Academy of Sciences Fujian Institute of Research on the Structure of Matter

Yun WANG

Chinese Academy of Sciences Fujian Institute of Research on the Structure of Matter

Xiaoyun Li

Chinese Academy of Sciences Fujian Institute of Research on the Structure of Matter

Zehua Zhou

Chinese Academy of Sciences Fujian Institute of Research on the Structure of Matter

Jian CHEN

Chinese Academy of Sciences Fujian Institute of Research on the Structure of Matter

Zhuguang LIU

Chinese Academy of Sciences Fujian Institute of Research on the Structure of Matter

Wang GUO

Chinese Academy of Sciences Fujian Institute of Research on the Structure of Matter

Research Article

Keywords: Y₂O₃, Sc₂O₃, Solid solution transparent ceramics, Thermal conductivity, mechanical properties

Posted Date: November 29th, 2021

DOI: <https://doi.org/10.21203/rs.3.rs-1113962/v1>

License: © ⓘ This work is licensed under a Creative Commons Attribution 4.0 International License.

[Read Full License](#)

Optical, thermal, and mechanical properties of $(Y_{1-x}Sc_x)_2O_3$ transparent ceramics

Changliang YANG^{a,b}, Jiquan HUANG^{a,b,c,*}, Qiufeng HUANG^b, Zhonghua DENG^{b,c}, Yun WANG^{a,b}, Xiaoyun Li^{a,b}, Zehua Zhou^{a,b}, Jian CHEN^{b,c}, Zhuguang LIU^{b,c}, Wang GUO^{b,c,*}

^aCollege of Chemistry and Materials, Fujian Normal University, Fuzhou 350007, P. R. China.

^bKey Laboratory of Optoelectronic Materials Chemistry and Physics, Fujian Institute of Research on the Structure of Matter, Chinese Academy of Sciences, Fuzhou, 350002, P. R. China. E-mail: hjq@ffirsm.ac.cn, guowang@ffirsm.ac.cn.

^cFujian Science & Technology Innovation Laboratory for Optoelectronic Information of China, Fuzhou, 350108, P. R. China.

Abstract: Sesquioxides such as Y_2O_3 and Sc_2O_3 are important optical materials, but the fabrication of their transparent ceramics remains a challenge due to the ultra-high melting point of over 2400 °C. In this work, a series of $(Y_{1-x}Sc_x)_2O_3$ transparent ceramics were successfully fabricated by a simple vacuum sintering process without any sintering additives, and the effect of Scandium (Sc) content on the crystal structure and optical/thermal/mechanical properties were evaluated. Y_2O_3 and Sc_2O_3 form a complete solid solution with a cubic bixbyite structure. The formation of $(Y_{1-x}Sc_x)_2O_3$ solid solution promotes the densification of ceramics, leading to the realization of high transparency close to the theoretical transmittance over a wide wavelength range of 0.35-8 μm . In particular, the in-line transmittance in the range of 0.6-6 μm remains above 80% for $(Y_{1-x}Sc_x)_2O_3$ with $x = 0.23-0.31$, while the pristine Y_2O_3 and Sc_2O_3 are opaque. Moreover, the mechanical properties including Vickers hardness (H_v), fracture toughness (K_{IC}), and biaxial strength (δ_b) are evidently enhanced due to the solid solution strengthening, while the thermal conductivity is reduced due to the reduction of photon free path. This study demonstrates that forming of solid solution is a facile and universal approach for preparing sesquioxides transparent ceramics with high optical and mechanical quality.

Keywords: Y_2O_3 ; Sc_2O_3 ; Solid solution transparent ceramics; Thermal conductivity;

mechanical properties.

1. Introduction

Y_2O_3 , Sc_2O_3 , and Lu_2O_3 are bixbyite-type sesquioxides crystals with the same cubic structure, and the space group is Ia-3 (206) [1]. These sesquioxides have similar physical and chemical properties, such as strong corrosion resistance, high thermal stability, high thermal conductivity (12-18 W/K·m), wide band-gap (5.6-6.0 eV), wide range of optical transparency wavelength (0.3-8 μm), low maximum phonon energy, and high refractive index (1.88-1.97) [1-4]. Owing to these superior characteristics, Y_2O_3 , Sc_2O_3 , and Lu_2O_3 are excellent scintillators and laser hosts, in particular, they are more suitable for high-performance and ultrafast laser applications than $\text{Y}_3\text{Al}_5\text{O}_{12}$ (YAG) [1,5]. Also, they are considered as promising candidates for the next generation of infrared (IR) windows operating in harsh environments [6]. However, their extremely high melting point (> 2400 °C) complicates the growth of single crystals and the fabrication of transparent ceramics with high quality and large size. Lowering down the synthesis temperature has thus become the most important solution. In this regard, an effective strategy, parallel to the improvement of sintering technology and powder engineering, is to introduce sintering additives. In the past decades, various sintering additives, such as LiF [7], CaO [8], ZrO_2 [9], HfO_2 [10], TiO_2 [11], and La_2O_3 [12], have been adopted to promote the densification of sesquioxide transparent ceramics at a sintering temperature far below the melting point, and it is found that the in-line transmittance and even the laser performances of the resultant ceramics can be comparable to those of single crystals [1]. However, the utilization of sintering additives also introduces secondary phases, which aggravates the scattering and decreases the quality of the transparent ceramics [13].

Recently, an alternative method of synthesizing sesquioxide transparent ceramics (and single crystals) has been proposed, which is to reduce the synthesis temperature by forming a solid solution [1,14]. It is found that Y_2O_3 , Sc_2O_3 , and Lu_2O_3 can be mixed in arbitrary ratios to form complete solid solution series with the formula of $(\text{Lu}_x\text{Y}_y\text{Sc}_{1-x-y})_2\text{O}_3$ ($0 \leq x < 1$, $0 \leq y < 1$, and $0 < x + y \leq 1$), and the melting (or liquidus) points of the binary and ternary systems are generally lower than that of any constituent component [1,14-17]. For example, the melting points of Y_2O_3 , Sc_2O_3 , and Lu_2O_3 are around 2450 °C, while those of their solid solution $(\text{Y}_{0.55}\text{Sc}_{0.45})_2\text{O}_3$, $(\text{Lu}_{0.55}\text{Sc}_{0.45})_2\text{O}_3$, $(\text{Lu}_{0.55}\text{Y}_{0.45})_2\text{O}_3$, and $(\text{Lu}_{0.2}\text{Y}_{0.4}\text{Sc}_{0.4})_2\text{O}_3$ are about 2050, 2350, 2340, and 2110 °C, respectively [1,14,15]. It is worth noting that the melting points of Y_2O_3 and Sc_2O_3 can be reduced by up to ~400 °C by forming a solid solution, which is conducive to the synthesis of

high-purity, high-quality transparent ceramics. Furthermore, Y_2O_3 is one of the most excellent hosts for mid-IR laser operation due to its lowest maximum phonon energy ($\sim 591\text{ cm}^{-1}$), while Sc_2O_3 possesses higher thermal capacity, thermal conductivity, and Young's modulus than Y_2O_3 [14]. The synergy of these advantages may occur in the $(Y_{1-x}Sc_x)_2O_3$ solid solution. In fact, several studies have shown that, for the solid solutions, not only ultrashort pulse laser and larger emission bandwidths than constituent sesquioxide can be achieved, but also the mechanical toughness and hardness can be enhanced [18,19]. Therefore, excellent optical and mechanical properties are highly anticipated in the (pristine and rare-earth-doped) Sc_2O_3 - Y_2O_3 solid solution.

In this work, with cheap commercial Y_2O_3 and Sc_2O_3 micron powders as starting materials, we fabricate a series of $(Y_{1-x}Sc_x)_2O_3$ transparent ceramics by the simple pressure-less sintering method, and investigate the influence of scandium content on the crystal structure, densification, optical transmittance, thermal and mechanical properties of the ceramics.

2. Experimental

2.1 Fabrication of $(Y_{1-x}Sc_x)_2O_3$ ceramics

High purity Y_2O_3 and Sc_2O_3 (99.99%) powders with particle sizes of 2-6 μm were used as starting materials. The oxide powders were mixed according to the formula of $(Y_{1-x}Sc_x)_2O_3$ ($0 \leq x < 0.5$), and ball-milled in absolute ethanol for 22 h. The as-obtained slurry was dried, then ground and sieved through a 100-mesh sieve. The powders were uniaxially compressed at 8 MPa to form a green body, and then cold isostatically pressed at 200 MPa for 1 minute. Subsequently, the $(Y_{1-x}Sc_x)_2O_3$ green bodies were vacuum sintered at 1800 °C for 20 h, followed by annealing at 1200 °C for 10 h in air. The as-obtained ceramics were mirror-polished to facilitate subsequent characterization.

2.2 Characterization

The phase composition of the ceramics was examined by powder X-ray diffraction (XRD, Mini Flex600, Rigaku, Japan) using $\text{Cu K}\alpha$ radiation. The theoretical density of the ceramics was calculated based on the XRD patterns, while the experimental bulk density was determined by the Archimedes method using absolute ethyl alcohol at room temperature. The morphology was observed by scanning electron microscope (SEM, SU-8010, Hitachi, Japan) and EDX was used to identify the chemical compositions. The optical transmittance (and reflection) was

measured by an ultraviolet-visible-near-infrared spectrophotometer (Lambda950, U.S. PE company) in the wavelength range of 0.2 - 2.5 μm , and infrared transmittance was measured by FT-IR Spectrometer (VERTEX 70, Bruker) ranging from 2.5 - 10 μm .

For thermal-expansion measurement, the samples were cut into 4 mm \times 3 mm \times 25 mm and measured on dilatometry DIL 402PC (NETZSCH, German). Thermal diffusion coefficient and specific heat of the transparent ceramic were measured by the laser flash method using a laser flash apparatus (LFA457, Nanoflash, Netzsch). For sample with isotropic cubic structure, the linear thermal expansion coefficient (α) can be calculated by the expression below [20]:

$$\alpha = \frac{1}{L_0} \frac{dL}{dT} \quad (1)$$

here, L_0 is the initial length of the specimen, dL is the change in length within the temperature interval dT . The thermal conductivity (k) as a function of temperature can be calculated using the following equation [21]:

$$k(T) = \lambda(T) \cdot \rho(T) \cdot C_p(T) \quad (2)$$

where $\lambda(T)$, $\rho(T)$, and $C_p(T)$ are the thermal diffusivity, density and heat capacity at Temperature T , respectively.

The Vickers hardness and fracture toughness of the $(\text{Y}_{1-x}\text{Sc}_x)_2\text{O}_3$ transparent ceramics (ϕ 20 mm \times 1 mm) were obtained from 20 indentations made by Digital Vickers Hardness Tester HV-1000IS (Jujing, shanghai). The flexure strengths were measured by the three-point bending method using machined ceramic bars (3 mm \times 4 mm \times 36 mm; five bars were measured for each sample) on a universal tester (Instron 1195, Instron, USA). The Vickers hardness (H_v) and fracture toughness (K_{IC}) are estimated by the generally accepted formulas [22]:

$$H_v = S \frac{P}{d^2} \quad (3)$$

and

$$K_{IC} = 0.018 \left(\frac{E}{H_v} \right)^{1/2} \left(\frac{P}{l^{3/2}} \right) \quad (4)$$

where d is the length of indentation diagonal; P is the load on the indenter, which is equal to 9.8 N; S is the shape factor of the indenter, which is equal to 1.854 for a pyramid-shaped indentation; E is the Young modulus, which is considered to be 179.8 GPa for Y_2O_3 [23]; $l = c - a$ (a is the length of the half-diagonal of the indent and c is the half-length of the indentation crack).

3. Results and discussion

The XRD patterns of the $(Y_{1-x}Sc_x)_2O_3$ ceramics, as well as the standard diffraction profiles of Y_2O_3 (JCPDS Card No.41-1105) and Sc_2O_3 (JCPDS Card No.42-1463), are presented in Fig. 1 and Fig.S1. For the pristine Y_2O_3 ceramic, all diffraction peaks matched well with the standard PDF #41-1105 (Fig. S1), and thus could be indexed in terms of the cubic bixbyite structure with space group Ia-3 (206). The incorporation of Sc_2O_3 into Y_2O_3 matrix resulted in the shift of diffraction peaks to a higher 2θ angle without the appearance of additional peaks (Fig. 1a), indicating the formation of Sc_2O_3 - Y_2O_3 complete solid solution series. It is reported that perovskite-type $YScO_3$ (rare earth scandate) can be obtained by calcining the raw materials (Sc_2O_3 - Y_2O_3 mixture) in the air at 1400 °C [24]. $YScO_3$ has orthogonal symmetry and has a birefringence effect at the grain boundary, which is harmful to the transparency of ceramics. Therefore, the partial formation of the perovskite phase should be avoided. As shown in Fig. 1a, diffraction peaks attributed to the perovskite structure did not appear in the XRD patterns of the $(Y_{1-x}Sc_x)_2O_3$ ceramics. The reason can be explained as follows. In the Ln_2O_3 - Sc_2O_3 (Ln stands for rare earth elements such as Y, La, Nd, Sm, Yb, Lu, etc.) system, as the radius of the Ln^{3+} ion decreases, the formation of the perovskite phase becomes increasingly difficult [25-27]. For example, perovskite compounds ($LnScO_3$) can be synthesized for larger Ln ions ranging from La to Tb, while for Ln = Er, Tm, Yb and Lu, only cubic solid solutions are formed. The ionic radius of Y^{3+} (as well as Dy^{3+} and Ho^{3+}) is between Tb^{3+} and Er^{3+} , therefore, the formation of $YScO_3$ (as well as $DyScO_3$ and $HoScO_3$) requires harsh conditions such as high pressure. The theoretical densities of perovskite-type $YScO_3$ and bixbyite-type $(Y_{0.5}Sc_{0.5})_2O_3$ solid solution are calculated to be 4.95 and 4.53 g/cm³, respectively, which means that the perovskite phase is preferred at higher pressure. Clark et.al. reported that cubic solid solution with trace of perovskite was formed after calcining the Y_2O_3 - Sc_2O_3 mixtures at ambient pressure (~1 bar) while single-phase $YScO_3$ was yielded at a higher pressure of 20 kbar [25]. In this work, $(Y_{1-x}Sc_x)_2O_3$ ceramics were vacuum sintered. The low pressure (~10⁻⁵ mbar) blocks the formation of the perovskite phase, which is conducive to the realization of a complete solid solution. Interestingly, we further treated these $(Y_{1-x}Sc_x)_2O_3$ ceramics at 1.8 kbar (180 MPa), 1700 °C for 3 h, and found that they remained cubic solid solution without forming

a perovskite phase (Fig. S2), which highlights the thermodynamic stability of the cubic bixbyite structure.

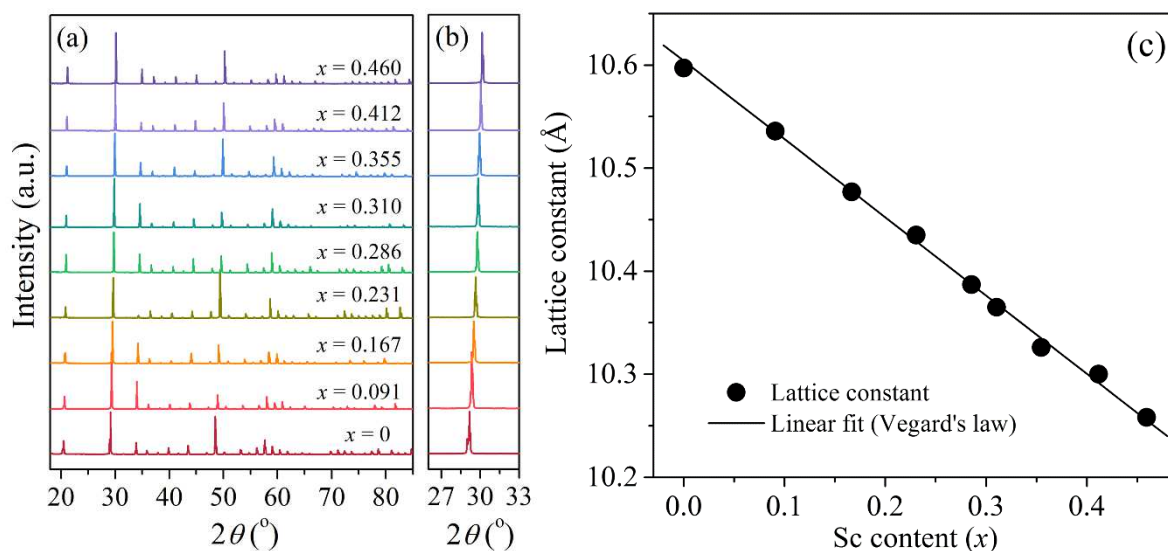


Fig.1 (a) XRD patterns of the $(Y_{1-x}Sc_x)_2O_3$ ceramics. (b) The enlarged patterns from 26.6 to 36.0° . (c) Dependence of the lattice constant on the Sc content. The solid line represents the fitting result calculated using the Vegard's law with an expression of $a(x) = xa_{Sc} + (1-x)a_Y$.

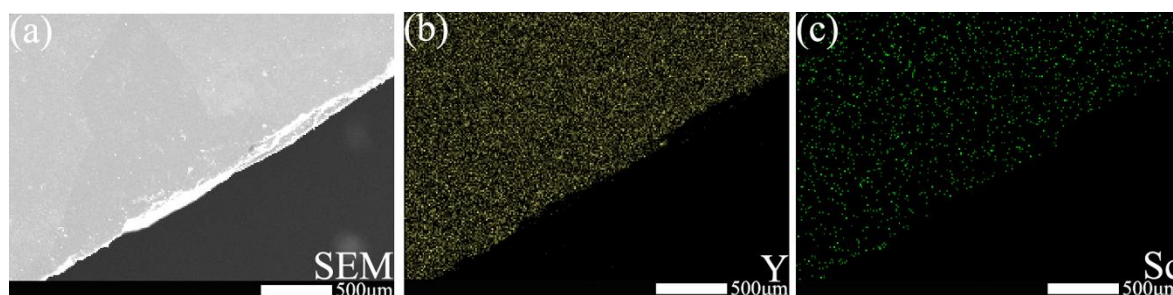


Fig.2 Surface SEM image of $(Y_{0.769}Sc_{0.231})_2O_3$ transparent ceramic (a), and the corresponding EDS mappings of Y (b) and Sc (c) elements.

For all the samples, their (222) peaks (located at $2\theta = 29-30.5^\circ$, as shown in Fig. 1b) were intensive and sharp, and the FWHM (full width at half maximum) was almost the same, indicating that the scandium element was uniformly distributed in the Y_2O_3 matrix, which was further demonstrated by the EDS observation. Fig. 2 shows the EDS elemental mapping of $(Y_{0.769}Sc_{0.231})_2O_3$ ceramic, both Y and Sc elements were homogeneous distributed, which highlighted the formation of $(Y_{1-x}Sc_x)_2O_3$ solid solution without local aggregation or second phases. As aforementioned, the diffraction peaks of $(Y_{1-x}Sc_x)_2O_3$ shifted to a higher 2θ angle with increasing Sc concentration (Fig. 1b), which was attributed to the decrease in the lattice constant. The effective ionic radius is 0.745 \AA for Sc^{3+} and 0.90 \AA for Y^{3+} in 6-coordinate

environments. Therefore, the substitution of Y^{3+} ions by smaller Sc^{3+} ions must result in the shrinkage of the unit cell. According to the XRD patterns, the lattice constant of $(Y_{1-x}Sc_x)_2O_3$ was calculated and presented in Fig. 1c. The lattice constant has a linear relationship with Sc concentration (x), and agrees well with the theoretical value calculated by Vegard's law, that is, $a(x) = xa_{Sc} + (1-x)a_Y$, where $a(x)$, a_{Sc} ($= 9.845 \text{ \AA}$) and a_Y ($= 10.604 \text{ \AA}$) are the lattice constants of $(Y_{1-x}Sc_x)_2O_3$, Sc_2O_3 and Y_2O_3 , respectively. We can thus conclude that Y and Sc elements are randomly distributed in the cation sites of the cubic lattice, and the lattice constant of the solid solutions follows the rule of mixture.

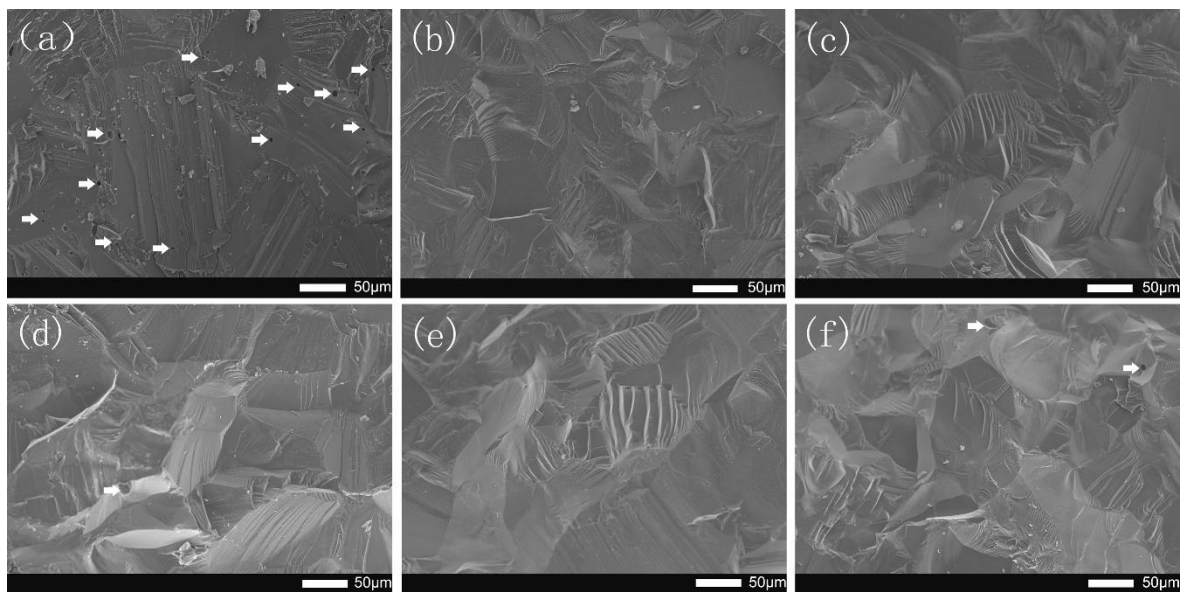


Fig. 3 Cross-sectional SEM images of $(Y_{1-x}Sc_x)_2O_3$ ceramics with $x = 0$ (a), 0.091 (b), 0.184 (c), 0.286 (d), 0.355 (e), and 0.412.

Fig. 3 presents the cross-sectional morphologies of the $(Y_{1-x}Sc_x)_2O_3$ ceramics. It is readily apparent that the microstructures of the samples are closely related to the content of Sc_2O_3 . As shown in Fig.3a, considerable residual pores were observed in the pristine Y_2O_3 ceramics. However, the pores were almost removed completely in the $(Y_{1-x}Sc_x)_2O_3$ ceramics with $x = 0.184-0.355$ (Fig. 3, panels c-e). As the Sc_2O_3 content further increased to 0.412, few pores appeared again (Fig. 3f). Obviously, the densification of Y_2O_3 ceramics can be effectively improved by incorporating an appropriate amount of Sc_2O_3 , which is beneficial to the fabrication of transparent ceramics. Fig. 4 shows the variation of the relative density of the $(Y_{1-x}Sc_x)_2O_3$ ceramics with Sc content (x). The relative density increased remarkably with x and reached the highest value of 99.79% when $x = 0.310$, above which the relative density turned

to decrease. The pronounced dependence of the porosity on composition is believed to be related to the change in melting point. To confirm this viewpoint, Fig. 4 also presents the binary phase diagram of the Y_2O_3 - Sc_2O_3 system with Sc_2O_3 content of 0-50% ($0 \leq x \leq 0.5$). It is found that the melting temperature drops sharply from 2430 °C of Y_2O_3 to below 2100 °C of $(Y_{1-x}Sc_x)_2O_3$ with $x > 0.18$, which is essential for improving the densification and transparency of the ceramics.

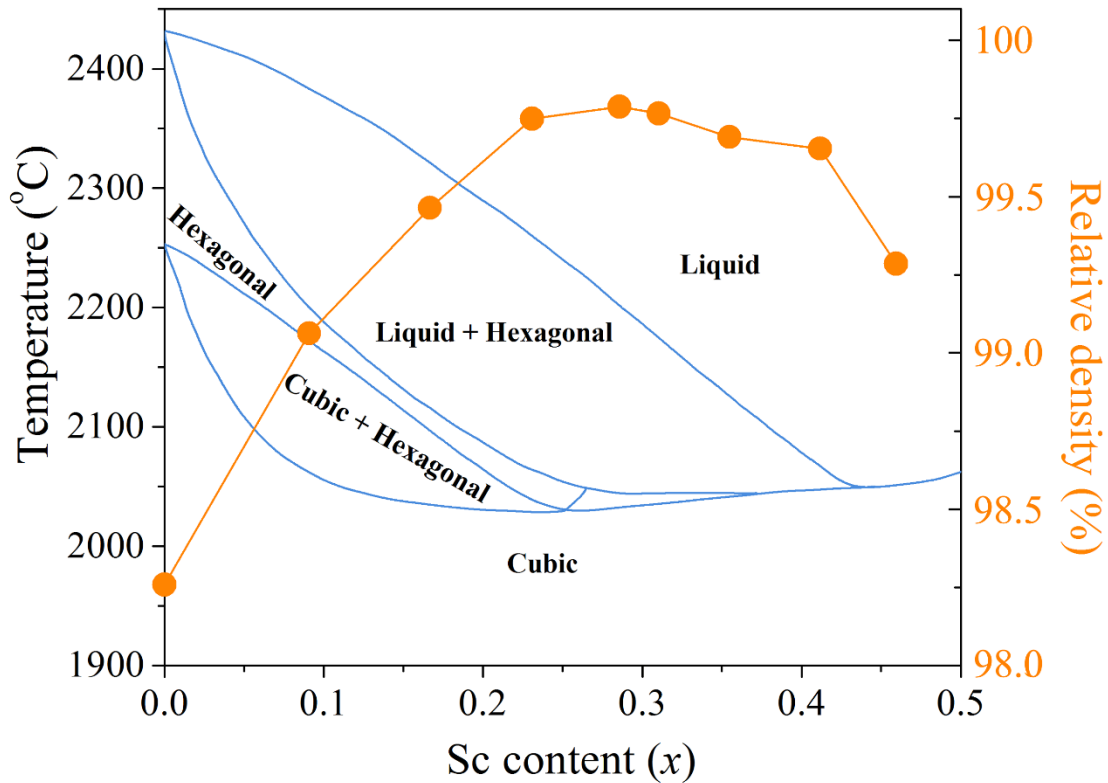


Fig.4 Relative density of the $(Y_{1-x}Sc_x)_2O_3$ transparent ceramics, and the phase diagram of binary Y_2O_3 - Sc_2O_3 system [3,16].

Fig.5a shows the photographs of the $(Y_{1-x}Sc_x)_2O_3$ ceramics with the same thickness of 1 mm, while Fig. 5b and 5c display their UV-Vis-NIR (200-2500 nm) and IR (2500-10000 nm) transmittance spectra, respectively. It is found that the optical transmittance of Y_2O_3 can be enhanced markedly by Sc-incorporating. The pristine Y_2O_3 ceramic was opaque (the in-line transmittance was lower than 1% within the visible region). However, for the $(Y_{1-x}Sc_x)_2O_3$ samples, with increasing Sc content, the transparency of the ceramics increased greatly and reached the maximum at $x \approx 0.286$, and then turned to decrease gradually, which was consistent with the observation of morphology and density (Fig. 3 and Fig. 4). With 16-36% Sc_2O_3 incorporation, the samples were highly transparent over a wide wavelength range of 350-8000

nm. For example, the in-line transmittance at 4000 nm was as high as 81.5%, 82.2%, 80.2%, 81.8%, and 79.6% for $(Y_{1-x}Sc_x)_2O_3$ samples with $x = 0.167, 0.231, 0.259, 0.286,$ and $0.310,$ respectively. Similarly, the transmittance of sample $(Y_{0.714}Sc_{0.286})_2O_3$ ($x = 0.286$) was 81.3%@600nm, 82.3%@2000nm, 81.8%@4000nm, and 81.7%@6000nm, respectively (Fig. 5d), which were close to the theoretical values of Y_2O_3 single crystal (81.9%@600nm and 82.4%@2000nm). The high transparency and the broad transparency range highlight the excellent quality of the $(Y_{1-x}Sc_x)_2O_3$ transparent ceramics.

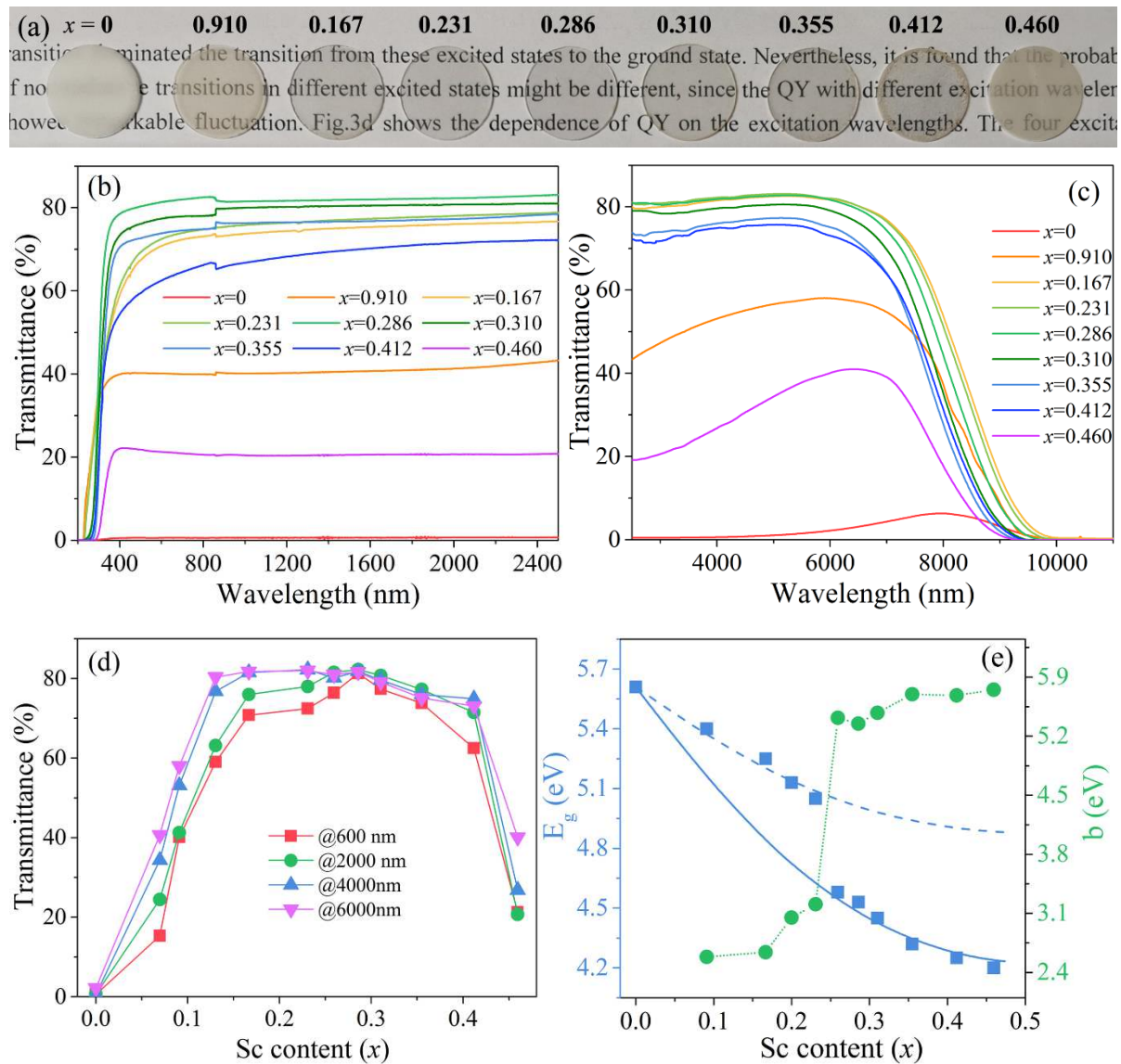


Fig.5 Photographs (a), and in-line UV-Vis (b) and IR (c) transmission spectra of the $(Y_{1-x}Sc_x)_2O_3$ ceramics. (d) Dependence of the transmittance at different wavelength on Sc contents. (e) Optical bandgap and bowing coefficient as plots of Sc contents. The solid and dash blue lines represent the fitting result with the expression of $E_g(x) = xE_g(Sc_2O_3) + (1-x)E_g(Y_2O_3) - bx(1-x)$ by setting $b = 5.6$ and 3.0 , respectively. The green dot line is only to guide the eye.

The transmittance of the $(Y_{1-x}Sc_x)_2O_3$ transparent ceramics exhibited a sharp decline in both the IR and UV regions. The IR cutoff was controlled by multi-phonon interactions, while the UV edge was attributed to the absorption across the band gap (i.e., the electronic transition from the valence band to conduction band) [28]. The optical band-gap (E_g) of the $(Y_{1-x}Sc_x)_2O_3$ ceramics was calculated from the UV cutoff curves by using the Tauc formula [29], and the results were presented in Fig. 5e. The value of E_g was 5.61 eV for Y_2O_3 and 5.65 eV for Sc_2O_3 , respectively (see Fig. S3). For the $(Y_{1-x}Sc_x)_2O_3$ ceramics, the band-gap decreased significantly with increasing Sc content. Especially, the value of E_g fell into the range of 4.2-4.6 eV when $x > 0.25$, which was far smaller than that of Y_2O_3 (and Sc_2O_3). The deviation of the experimental values from Vegard's law can be attributed to the band-gap bowing effect [30, 31]. For isovalent semiconductor (or insulator) compounds $A_xB_{1-x}C$, because of the atomic size and orbital energy differences between A and B, the local crystal symmetry is distorted, and isovalent defect levels may also be induced [32,33]. As a result, the band-gap is narrowed, which is manifested as the downward bowing of the curve of band-gap $E_g(x)$ versus molar fraction x . Such band-gap bowing can be described by a quadratic equation: $E_g(x) = xE_g(AC) + (1-x)E_g(BC) - bx(1-x)$, where b is the bowing parameter, $E_g(AC)$ and $E_g(BC)$ are the band-gaps of the constituents AC and BC, respectively [33,34]. As shown in Fig.5e, with increasing Sc content (x), b increased slightly when $x < 0.23$ and when $x > 0.26$, but increased sharply (from ~3.0 to ~5.4 eV) around $x = 0.25$. This phenomenon is analogous to the percolation effect. The percolation effect can be simply understood as an abrupt change of a certain physical property (such as dielectric constant, elastic modulus, electrical conductivity, and thermal conductivity) near the percolation threshold. The percolation threshold (x_p) is a mathematical concept that describes the formation of long-range connectivity in random networks, which is defined as the critical value of the occupation probability (or the minimum fraction of the occupied sites) forming an infinite connected cluster [35,36]. For example, an infinite chain of Sc-O-Sc-O bonds forms in the $(Y_{1-x}Sc_x)_2O_3$ solid solution when $x \geq x_p$, while only isolated Sc-O bonds or finite Sc-O-Sc-O chains exist when $x < x_p$. As shown in Fig. 5e, the b value has a sudden change near $x = 0.25$ for $(Y_{1-x}Sc_x)_2O_3$, which is consistent with the theoretical value of $x_p = 0.245$ for bcc Bravais lattice. However, at present, there is not enough evidence to prove that the band-gap bowing is related to the percolation effect.

In addition to the optical properties, thermal and mechanical performances are also important indicators for transparent ceramics. Fig. 6a shows the dependence of thermal expansion (dL/L_0) on temperature. Since the dilatometer furnace was not stable around room temperature and at the initial stage, the thermal expansion coefficients were not accurate below 500 K. At temperature above 500 K, the thermal expansion curves were essentially linear, and was almost independent of composition. For example, the values of dL/L_0 at 900 K was 0.00427, 0.00446, 0.00458, 0.00448 and 0.00447 for $(Y_{1-x}Sc_x)_2O_3$ with $x = 0, 0.167, 0.286, 0.355,$ and 0.460 , respectively. Fig. 6b plots the thermal expansion coefficient (α) versus temperature for the $(Y_{1-x}Sc_x)_2O_3$ samples. It was found that the incorporation of Sc resulted to a slight increase in the thermal expansion coefficient, which can be attributed to the higher thermal expansion coefficient of Sc_2O_3 relative to Y_2O_3 [14].

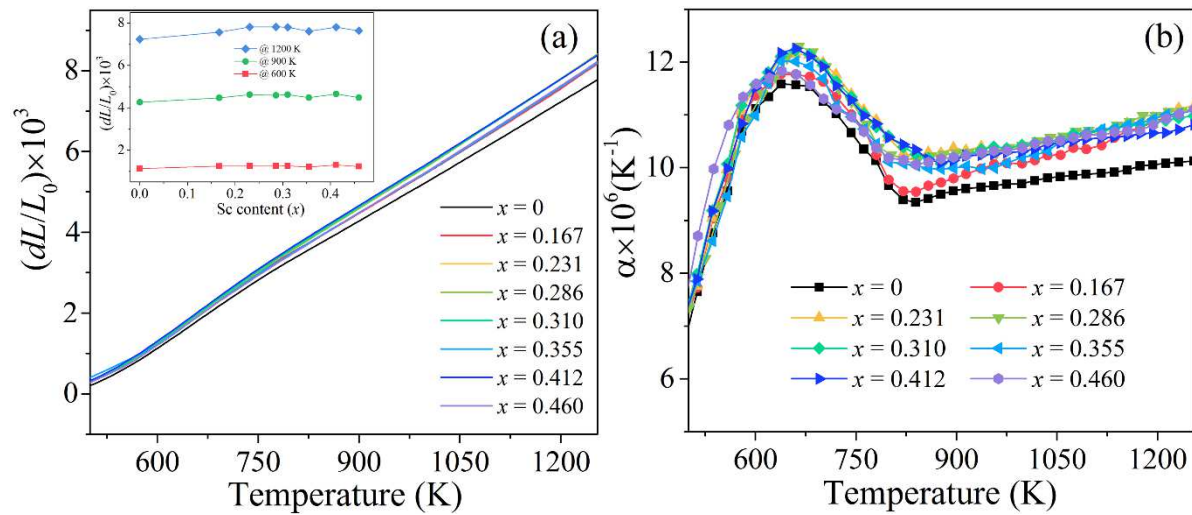


Fig.6 (a) Thermal expansion and (b) thermal expansion coefficient of the $(Y_{1-x}Sc_x)_2O_3$ transparent ceramics as a function of temperature. The inset in (a) shows the dependence of the thermal expansion on Sc content under different temperatures.

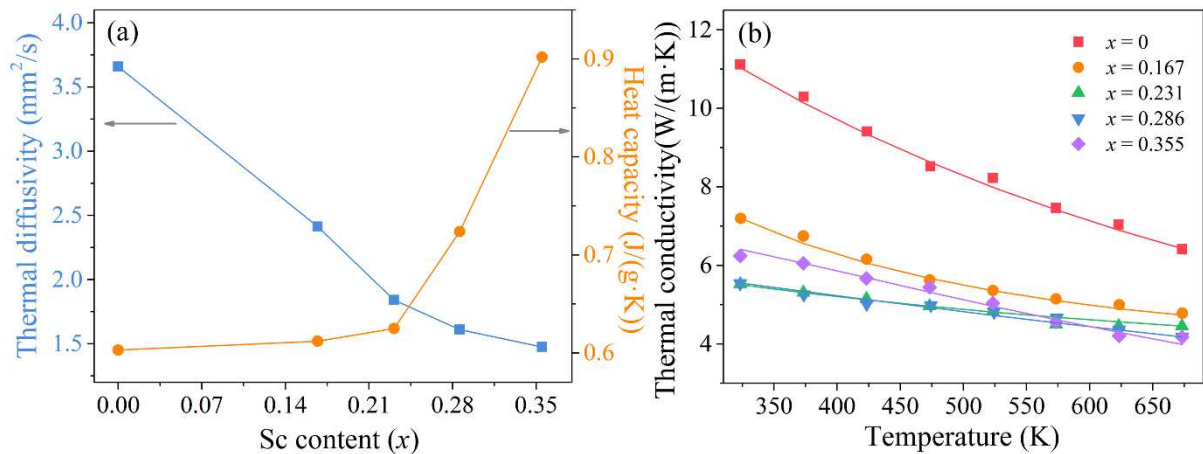


Fig.7 (a) Dependence of the room temperature thermal diffusivity and heat capacity of the the $(Y_{1-x}Sc_x)_2O_3$ transparent ceramics on Sc contents, (b) thermal conductivity of the $(Y_{1-x}Sc_x)_2O_3$ transparent ceramics as a function of temperature. The solid lines represent the fitting results calculated using Eq. (5).

Fig. 7a shows the variations of the heat capacity (C_p) and thermal diffusivity (λ) of the $(Y_{1-x}Sc_x)_2O_3$ transparent ceramics with Sc content. The thermal diffusivity decreased monotonically with increasing Sc content, from 3.66 mm²/s for pristine Y_2O_3 ($x = 0$) to 1.48 mm²/s for $(Y_{0.645}Sc_{0.355})_2O_3$ ($x = 0.355$). In contrast, since the heat capacity of Sc_2O_3 is higher than that of Y_2O_3 [14], the addition of Sc increases the heat capacity of the sample. According to the empirical Neumann-Kopp rule [30], the heat capacity of the $(Y_{1-x}Sc_x)_2O_3$ solid-state solution is approximately equal to the stoichiometric sum of the respective capacities of Sc_2O_3 and Y_2O_3 .

Based on the experimental determined thermal diffusivity, heat capacity and density, the thermal conductivity (k) of the $(Y_{1-x}Sc_x)_2O_3$ ceramics was calculated by Eq.(2) and displayed in Fig. 7b. The thermal conductivity decreased with increasing temperature, which can be well described by the following equation [21,31]:

$$k(T) = \frac{1}{a+bT+cT^2} \quad (5)$$

where a , b , and c are constants. It therefore implies that the thermal conductivity is dominated by four-phonon heat transport [21]. The phonon mean free path is reduced by the phonon scattering and goes as $1/T$ above the Debye temperature, which causes the thermal conductivity to decrease at higher temperatures [31]. Meanwhile, due to the mismatch of atomic mass and ionic radius between Y^{3+} and Sc^{3+} , the incorporation of Sc into the Y_2O_3 matrix will cause structural deformation, which also reduces the phonon mean free path. As a result, the room temperature thermal conductivity was decreased from 11.12 W/(m·K) for pristine Y_2O_3 ($x = 0$) to 7.20, 5.53, 5.55, and 6.24 W/(m·K) for $(Y_{1-x}Sc_x)_2O_3$ with $x = 0.167, 0.231, 0.286, \text{ and } 0.355$, respectively, as shown in Fig. 7b. According to Eq.(2), the thermal conductivity is determined by the thermal diffusivity, density and heat capacity. As aforementioned, with increasing Sc content, both the diffusivity and density decrease, which reduces the thermal conductivity. However, the heat capacity increases, which improves the thermal conductivity. Consequently, the overall decrease in thermal conductivity is limited greatly. It is noted that the thermal

conductivity of the $(Y_{1-x}Sc_x)_2O_3$ transparent ceramics is comparable with that of Y_2O_3 ceramics doped with rare-earth (such as 0.5%Nd: Y_2O_3) [22] and with sintering aid (such as 2.72wt% ZrO_2 doped Y_2O_3) [11], and higher than that of traditional laser glass.

Table 1 A summary of the Vickers hardness (H_v), fracture toughness (K_{IC}), biaxial strength (δ_b), damage tolerance (D_t), and brittleness index (B) of the $(Y_{1-x}Sc_x)_2O_3$ ceramics.

Sc content (x)	H_v (GPa)	K_{IC} (Mpa·m ^{1/2})	δ_b (MPa)	D_t (m ^{1/2})	B ($\mu\text{m}^{-1/2}$)
0	6.71 ± 0.01	1.16 ± 0.12	81.48	0.379	5.78
0.091	8.04 ± 0.14	1.27 ± 0.07	94.22	0.300	6.33
0.167	8.42 ± 0.17	1.39 ± 0.09	96.38	0.307	6.06
0.231	9.44 ± 0.10	1.56 ± 0.11	106.64	0.277	6.05
0.286	9.69 ± 0.14	1.40 ± 0.08	111.76	0.231	6.92
0.310	9.62 ± 0.16	1.21 ± 0.14	120.86	0.186	7.95
0.355	9.55 ± 0.01	1.11 ± 0.06	92.39	0.225	8.60
0.412	9.45 ± 0.14	1.32 ± 0.17	92.54	0.270	7.16

Good mechanical properties and damage tolerance are of great significance to the reliability and machinability of ceramics. Several key mechanical performance indicators, including the Vickers hardness (H_v), fracture toughness (K_{IC}), and biaxial strength (δ_b), are summarized in Table 1. It is found that $(Y_{1-x}Sc_x)_2O_3$ solid solutions have more excellent mechanical performances than the constituent oxides. For example, the Vickers hardness of $(Y_{1-x}Sc_x)_2O_3$ with $x = 0.231$, 0.286 and 0.310 was about 9.44, 9.69, and 9.62 GPa, respectively, which was much higher than that of Y_2O_3 (6.71 GPa) and Sc_2O_3 (6.75 GPa). The fracture toughness increased from 1.16 Mpa·m^{1/2} for pristine Y_2O_3 (and 1.21 Mpa·m^{1/2} for Sc_2O_3) to 1.56 Mpa·m^{1/2} for sample with $x = 0.231$ (and 1.40 Mpa·m^{1/2} for $x = 0.286$). Similarly, the biaxial strength of $(Y_{1-x}Sc_x)_2O_3$ with $x = 0.231$, 0.286 and 0.310 were 31%, 37% and 48% higher than that of Y_2O_3 , respectively. The improved mechanical properties can be attributed to the solid solution strengthening originating from lattice distortion [37,38]. Ideally, all atoms of a crystalline material locate perfectly in their lattice sites. However, for a solid solution such as $(Y_{1-x}Sc_x)_2O_3$, larger Y atoms push away their neighbors while smaller Sc atoms have extra space for movement. The difference in the atomic size (or ionic radius) of Y and Sc will inevitably cause the fluctuation of atoms from their perfect sites [39]. The resultant lattice distortion impedes dislocation movement, which enhances lattice strain and provides excess strength [39,40].

Hardness and fracture toughness are important material parameters describing the resistance to deformation and crack propagation, and their ratio quantifies the brittleness [41,42], i.e.,

$$B = \frac{H_v}{K_{IC}} \quad (6)$$

The brittleness index B can be used to quantitatively measure the machinability of ceramics. As shown in Table 1, the brittleness of the $(Y_{1-x}Sc_x)_2O_3$ solid solutions was higher than that of pristine Y_2O_3 , which is related to the aggravated lattice distortion. As mentioned earlier, lattice distortion suppresses the movement of dislocations, makes deformation difficult, and makes ceramics more brittle.

On the other hand, neither brittleness nor fracture toughness alone can characterize the damage tolerance of a material. The damage tolerance is a property of a structure relating to its ability to sustain defects safely. According to the general definition proposed by Bao *et al.* [43], the damage tolerance D_t can be expressed as following:

$$D_t = \frac{K_{IC}}{\delta_b} \cdot \frac{E}{H_v} \quad (7)$$

where the K_{IC}/δ_b ratio indicates the degree of crack tolerance, while the E/H_v item represents the capacity of energy dissipation. The calculated D_t values of the $(Y_{1-x}Sc_x)_2O_3$ ceramics were listed in Table 1. The formation of solid solution reduces the damage tolerance. For example, the value of damage tolerance was 0.379 and 0.231 $m^{1/2}$ for samples with $x = 0$ and 0.286, respectively. The lower D_t values indicate that the solid solutions are more sensitive to defects and surface impact. Nevertheless, the damage tolerance of most $(Y_{1-x}Sc_x)_2O_3$ ceramics is still higher than that of SiC (0.113 $m^{1/2}$), ZrO_2 (0.194 $m^{1/2}$), and Al_2O_3 (0.255 $m^{1/2}$) [43]. The high hardness and fracture toughness, as well as acceptable damage tolerance, indicating that the $(Y_{1-x}Sc_x)_2O_3$ transparent ceramics are capable of working in certain harsh environments.

4. Conclusions

In summary, using commercial Y_2O_3 and Sc_2O_3 powders as the starting materials, $(Y_{1-x}Sc_x)_2O_3$ transparent ceramics were successfully fabricated by the traditional solid state reaction in vacuum without any sintering additives. The experimental results show that Y_2O_3 and Sc_2O_3 can form a complete solid solution that crystallizing in cubic bixbyite phase by high-temperature treatment. For the $(Y_{1-x}Sc_x)_2O_3$ solid solution series, with increasing Sc content,

both the lattice constant and optical band-gap decrease. The decrease of lattice constant obeys the rule of mixtures, while the change in the band-gap deviates from the rule of mixtures, and the band-gap bowing is large and composition dependent.

The formation of $(Y_{1-x}Sc_x)_2O_3$ solid solution greatly reduces the melting point and effectively promotes the densification of the ceramics. The pristine Y_2O_3 ceramic is opaque, while the $(Y_{1-x}Sc_x)_2O_3$ solid solution ceramic becomes more and more transparent with the increase of Sc content (x), and achieve the highest transparency that almost equal to the theoretical transmittance of Y_2O_3 single-crystal at $x = 0.286$. This $(Y_{0.714}Sc_{0.286})_2O_3$ sample exhibits a wide optically transparent wavelength range between 0.35 and 8 μm , and its in-line transmittance remains above 81% in the range of 0.6-6 μm , highlighting its advantages as laser host and window material. In terms of thermal performance, the thermal expansion coefficient is almost independent of the composition, and the heat capacity increases with the increase of Sc content, but due to the decrease of the photon mean free path, the thermal conductivity of $(Y_{1-x}Sc_x)_2O_3$ ceramics still has a certain degree of decline. On the other hand, the mechanical properties including Vickers hardness, fracture toughness, and biaxial strength are enhanced effectively due to the solid solution strengthening. However, the $(Y_{1-x}Sc_x)_2O_3$ solid solution ceramics exhibit smaller damage tolerance and higher brittleness than Y_2O_3 , even though they also possess higher fracture toughness, which requires further improvement in the future work.

Acknowledgements

This research was supported by Fujian Science & Technology Innovation Laboratory for Optoelectronic Information of China (2021ZZ113) and the Strategic Priority Research Program of Chinese Academy of Sciences (XDA22010301)

References

- [1] Liu Z, Ikesue A, Li J. Research progress and prospects of rare-earth doped sesquioxide laser ceramics, *J Eur Ceram Soc* 2021, **41**: 3895-3910.
- [2] Zhang L, Yang J, Yu H, et al. High performance of La-doped Y_2O_3 transparent ceramics, *J Adv Ceram* 2020, **9**: 493-502.
- [3] Kränkel C, Uvarova A, Haurat É, et al. Czochralski growth of mixed cubic sesquioxide crystals in the ternary system Lu_2O_3 - Sc_2O_3 - Y_2O_3 , *Acta Crystallogr Sect B: Struct Sci Cryst Eng Mater* 2021, **77**: 550-558.
- [4] Xiao Z, Yu S, Li Y, et al. Materials development and potential applications of transparent ceramics: A review, *Mater Sci Eng* 2020, **139**: 100518.
- [5] Yavetskiy RP, Balabanov AE, Parkhomenko SV, et al. Enculescu, Effect of starting

- materials and sintering temperature on microstructure and optical properties of Y_2O_3 : Yb^{3+} 5 at% transparent ceramics, *J Adv Ceram* 2020, **10**: 49-61.
- [6] Liu L, Morita K, Suzuki TS, et al. Synthesis of highly-infrared transparent Y_2O_3 -MgO nanocomposites by colloidal technique and SPS, *Ceram Int* 2020, **46**: 13669-13676.
- [7] Majima K, Niimi N, Watanabe M, et al. Effect of LiF addition on the preparation and transparency of vacuum hot pressed Y_2O_3 , *Mater Trans JIM* 1994, **9**: 645-650.
- [8] Yin D, Wang J, Ni M, et al. Fabrication of Highly Transparent Y_2O_3 Ceramics with CaO as Sintering Aid, *Mater* 2021, **14**: 14020444.
- [9] Hou X, Zhou S, Li W, et al. Study on the effect and mechanism of zirconia on the sinterability of yttria transparent ceramic, *J Eur Ceram Soc* 2010, **30**: 3125-3129.
- [10] Osipov VV, Orlov AN, Maksimov RN, et al. The influence of HfO_2 additives on the optical of Nd^{3+} -doped Y_2O_3 ceramics, *Phys Status Soli C* 2013, **6**: 914-917.
- [11] Li X, Zhu Q, Xu Y, et al. Optical and thermal properties of TiO doped Y_2O_3 transparent ceramics synthesized by hot isostatic pressing, *J Am Ceram Soc* 2019, **104**: 2021-2028.
- [12] Gan L, Park YJ, Zhu LL, et al. Fabrication and properties of La_2O_3 -doped transparent yttria ceramics by hot-pressing sintering, *J Alloys Compd* 2017, **695**: 2142-2148.
- [13] Osipov VV, Shitov VA, Maksimov RN, et al. Properties of transparent Re^{3+} : Y_2O_3 ceramics doped with tetravalent additives, *Opt Mater* 2015, **50**: 65-70.
- [14] Pirri A, Toci G, Patrizi B, et al. Yb^{3+} :($\text{Lu}_x\text{Y}_{1-x}$) $_2\text{O}_3$ mixed sesquioxide ceramics for laser applications. Part I: Fabrication, microstructure and spectroscopy, *J Alloys Compd* 2021, **869**: 159227.
- [15] Chisty IL, Fabelinskii IL, Kitaeva VF, et al. Experimental study of the properties of ZrO_2 - Y_2O_3 and HfO_2 - Y_2O_3 solid solutions, *J Raman Spectrosc* 1977, **3**: 183-192.
- [16] Badie JM, Foex M. Determination experimentale, calcul er prevision de certains diagrammes Sc_2O_3 - Ln_2O_3 , *J Sol State Chem* 1978, **26**: 311-319.
- [17] Badie JM, High-temperature phases and phase-transitions in the systems Sc_2O_3 - Ln_2O_3 (Ln = lanthanide and yttrium), *Rev Int Hautes Temp Refract Fr* 1978, **15**: 183-189.
- [18] Du P, Huo D, Xi H, et al. Fabrication of nanocrystalline Sc_2O_3 - Y_2O_3 solid solution ceramics by spark plasma sintering, *Ceram Int* 2017, **43**: 9854-9859.
- [19] Zhang X, Gao S, Gui W, et al. First-principles study of structure, mechanical and optical properties of La- and Sc-doped Y_2O_3 , *J Rare Earths* 2019, **37**: 879-885.
- [20] Deng DQ, Xu L. Measurements of thermal expansion coefficient of phenolic foam at low temperatures, *Cryogenics* 2003, **43**: 465-468.
- [21] Gugushev C, Hidde J, Gesing TM, et al. Czochralski growth and characterization of $\text{Tb}_x\text{Gd}_{1-x}\text{ScO}_3$ and $\text{Tb}_x\text{Dy}_{1-x}\text{ScO}_3$ solid-solution single crystals, *CrystEngComm* 2018, **20**: 2868-2876.
- [22] Zhang L, Pan W. Structural and Thermo-Mechanical Properties of Nd: Y_2O_3 Transparent Ceramics, *J Am Ceram Soc* 2015, **98**: 3326-3331.
- [23] Yeheskel O, Tevet O. Elastic moduli of transparent yttria, *J Am Ceram Soc* 1999, **82**: 136-166.
- [24] Shimizu Y, Ueda K. Phase formation and UV luminescence of Gd^{3+} doped perovskite-type YScO_3 , *J Sol State Chem* 2016, **242**: 170-174.
- [25] Clark JB, Richter PW, Toit LD, High-pressure synthesis of YScO_3 , HoScO_3 , ErScO_3 , and TmScO_3 , and a reevaluation of the lattice constants of the rare earth scandates, *J Sol State*

- Chem* 1978, **23**: 129-134.
- [26] Giaquinta DM, Hans CL. Structural Predictions in the ABO_3 Phase Diagram, *Chem Mater* 1994, **6**: 365-372.
- [27] Uecker R, Velickov B, Klimm D, et al. Properties of rare-earth scandate single crystals (Re = Nd – Dy), *J Cryst Growth* 2008, **310**: 2649-2658.
- [28] Wei GC, Transparent ceramic lamp envelope materials, *J Phys D: Appl Phys* 2005, **38**: 3057-3065.
- [29] Tauc J, Grigorovi R, Vancu A. Optical properties and electronic structure of amorphous germanium, *phys stat sol* 1966, **15**: 627-637.
- [30] He H, Cao Y, Fu R, et al. Band gap energy and bowing parameter of In-rich InAlN films grown by magnetron sputtering, *Appl Surf Sci* 2010, **256**: 1812-1816.
- [31] Koide Y, Itoh H, Khan MRH, et al. Energy band-gap bowing parameter in an $Al_xGa_{1-x}N$ alloy, *J Appl phys* 1987, **69**: 4540-4543.
- [32] Wei SH, Zunger A. Giant and composition-dependent optical bowing coefficient in GaAsN alloys, *Phys Rev Lett* 1996, **76**: 663-667
- [33] Moon CY, Wei SH, Zhu YZ, et al. Band-gap bowing coefficients in large size-mismatched II-VI alloys: First-principles calculations, *Phys Rev B* 2006, **74**: 233202.
- [34] Shi HL, Duan YF. Band-gap bowing and p-type doping of (Zn, Mg, Be)O wide-gap semiconductor alloys a first-principles study, *Eur Phys J B* 2008, **66**: 439-444.
- [35] Nan CW, Physics of inhomogeneous inorganic materials, *Prog Mater Sci* 1993, **37**: 1-116.
- [36] Bellaiche L, Wei SH, Zunger A. Localization and percolation in semiconductor alloys: GaAsN vs GaAsP, *Phys Rev B* 1996, **54**: 17568-17576.
- [37] Senkov ON, Scott JM, Senkova SV, et al. Microstructure and room temperature properties of a high-entropy TaNbHfZrTi alloy, *J Alloy Compd* 2011, **509**: 6043-6048.
- [38] Gypen LA, Deruttere A. Multi-component solid solution hardening, *J Mater Sci* 1977, **12**: 1028-1033.
- [39] Tsai MH, Yeh JW. High-Entropy Alloys: A Critical Review, *Mater Res Lett* 2014, **2**: 107-123.
- [40] Xiang H, Xing Y, Dai FZ, et al. High-entropy ceramics: Present status, challenges, and a look forward, *J Adv Ceram* 2021, **10**: 385-441.
- [41] Boccaccini AR, Machinability and brittleness of glass-ceramics, *J Mater Process Technol* 1997, **65**: 302-304.
- [42] Lawn BR, Marshall DB. Hardness, toughness, and brittleness: an indentation analysis, *J Am Ceram Soc* 1979, **62**: 347-350.
- [43] Bao YW, Hu CF, Zhou YC. Damage tolerance of nanolayer grained ceramics and quantitative estimation, *Mater Sci Technol* 2013, **22**: 227-230.

Tables and Captions

Table 1. A summary of the Vickers hardness (H_v), fracture toughness (K_{IC}), biaxial strength (δ_b), damage tolerance (D_t), and brittleness index (B) of the $(Y_{1-x}Sc_x)_2O_3$ ceramics.

Figures and Captions

Captions

Fig.1 (a) XRD patterns of the $(Y_{1-x}Sc_x)_2O_3$ ceramics. (b) The enlarged patterns from 26.6 to 36.0°. (c) Dependence of the lattice constant on the Sc content. The solid line represents the fitting result calculated using the Vegard's law with an expression of $a(x) = xa_{Sc} + (1-x)a_Y$.

Fig.2 Surface SEM image of $(Y_{0.769}Sc_{0.231})_2O_3$ transparent ceramic (a), and the corresponding EDS mappings of Y (b) and Sc (c) elements.

Fig. 3 Cross-sectional SEM images of $(Y_{1-x}Sc_x)_2O_3$ ceramics with $x = 0$ (a), 0.091 (b), 0.184 (c), 0.286 (d), 0.355 (e), and 0.412.

Fig.4 Relative density of the $(Y_{1-x}Sc_x)_2O_3$ transparent ceramics, and the phase diagram of binary Y_2O_3 - Sc_2O_3 system

Fig.5 Photographs (a), and in-line UV-Vis (b) and IR (c) transmission spectra of the $(Y_{1-x}Sc_x)_2O_3$ ceramics. (d) Dependence of the transmittance at different wavelength on Sc contents. (e) Optical bandgap and bowing coefficient as plots of Sc contents. The solid and dash blue lines represent the fitting result with the expression of $E_g(x) = xE_g(Sc_2O_3) + (1-x)E_g(Y_2O_3) - bx(1-x)$ by setting $b = 5.6$ and 3.0, respectively. The green dot line is only to guide the eye.

Fig.6 (a) Thermal expansion and (b) thermal expansion coefficient of the $(Y_{1-x}Sc_x)_2O_3$ transparent ceramics as a function of temperature. The inset in (a) shows the dependence of the thermal expansion on Sc content under different temperatures.

Fig.7 (a) Dependence of the room temperature thermal diffusivity and heat capacity of the $(Y_{1-x}Sc_x)_2O_3$ transparent ceramics on Sc contents, (b) thermal conductivity of the $(Y_{1-x}Sc_x)_2O_3$ transparent ceramics as a function of temperature. The solid lines represent the fitting results calculated using Eq. (5).

Supplementary Files

This is a list of supplementary files associated with this preprint. Click to download.

- [Supportinginformation.docx](#)